

Real-time Micro-vascular Video Analysis

Chao Liu, Hernando Gomez, Srinivasa Narasimhan, Artur Dubrawski, Michael R. Pinsky

Abstract—Microcirculatory monitoring has been increasingly recognized as a valuable tool in the assessment of perfusion status of critically ill patients. Currently, Sidestream Dark Field (SDF) and Incident Dark Field (IDF) imaging represent the most recent advances in microcirculatory imaging, allowing for the real-time visualization of the capillary bed and its physiologic characteristics at the bedside. The potential to impact care of critically ill patients is evident, as this technology has opened an entire new dimension for the study and interpretation of peripheral perfusion, which is the guide and goal of every resuscitation effort in clinical medicine. However, despite that off line data extracted from these videos is clinically useful, the advantage of real-time imaging acquisition is currently faulted by the fact that analysis cannot be performed in such an instantaneous fashion. Several obstacles such as subsurface scattering within the tissue that surrounds the capillaries, transparency of plasma, imaging noise and lack of features amongst many others, have rendered current analysis of this information time-consuming and relatively subjective as it is dependent on manual operation and training in the interpretation of blood flow velocity. Accordingly, in this paper, we present a framework that automates the analysis process. Our method includes stages of video stabilization, enhancement, and micro-vessel extraction, and automatically yields estimate statistics of the microvascular blood flow. We have validated this method in animal experiments conducted carefully to record microcirculatory blood flow in animals before, during and after controlled hemorrhage, as well as after fluid resuscitation. We have been able to extract clinically-relevant data like blood flow velocity distribution, in real time, thus providing a novel methodology for real-time assessment of microcirculatory physiology that may serve to diagnose pathologic alterations and perhaps, to drive therapeutic interventions.

Index Terms—Micro-circulatory analysis, video processing, imaging, real-time, critical care

I. INTRODUCTION

Microcirculation takes place in part of the circulatory system embedded in tissue that involves the smallest vessels and where diffusion of nutrients and oxygen into the cells and removal of CO_2 and waste from the cells take place. Monitoring of microcirculation is useful for diagnosing of vascular conditions and in monitoring patients for cardio-respiratory insufficiency.

Sidestream Dark Field (SDF) [7] video imaging was developed as a non-invasive imaging approach for real-time visualization of superficial microvascular flow. However, analysis of these videos is currently limited by manual or semi-manual operation and coarse sampling techniques, which makes quantitative analysis of microcirculatory status and response to disease and treatment difficult and subjective [8]. We aim to remedy that. One of the portable SDF imaging devices is shown in Fig. 1(a). As depicted in Fig. 1(c), illumination is provided by the green light-emitting diodes (LEDs) arranged in a ring formation. The wavelength ($\lambda=530$ nm) of the illumination is chosen to maximize light absorption by the

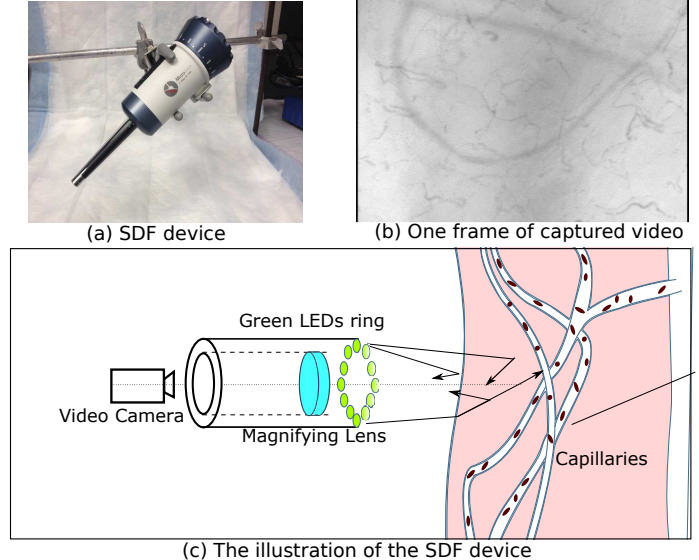


Fig. 1: Sidestream Dark Field Imaging[7]. (a) Portable SDF imaging device used for microcirculatory monitoring. (b) One frame of the microcirculatory video. (c) The LEDs, arranged and optically isolated around the lens system, emit light optimized for red blood cell absorption. Due to defocus, subsurface scattering of light, sensor noise, sensor drifting and limited texture of the tissue, it is not easy to extract physiological features from the SDF video.

red blood cells (RBCs). The tissue embedding the capillaries scatters and reflects the illumination back to the camera, making the capillaries imaged as dark curvilinear structures against the brighter background. The LEDs and the lens system are optically isolated to prevent the illumination generated by the LEDs from contaminating the images.

Despite that the design is optimized for microcirculatory imaging, as shown in Fig. 1(b), it is not easy to extract physiological features from SDF videos, such as the blood flow velocity, for several reasons: (1) Subsurface scattering: scattering of light on the path from the capillaries to the camera increase observed intensity of the vessels, reducing contrast of the images; (2) Defocus: capillaries are embedded at varied depths within the tissue while the depth of field of the camera is fixed to obtain desired magnification. So some capillaries in the field of view appear blurred, making their features more difficult to estimate; (3) Sensor noise that further reduces quality of images; (4) Limited texture: low diameter capillaries of interest comprise only a small part of the image, most of it is occupied by tissue without substantial texture and in addition, plasma in the capillaries is transparent, reducing texture in the frames even further, so traditional texture-based

image feature extraction methods will likely fail; (5) Sensor drift during video capture: field of view changes due to the motions induced by heart beat and respiration of the subject and movement of the device itself, relative to the observed tissue.

In this paper, we present an end-to-end, automated framework for real-time analysis of micro-circulation including vessel detection, heart rate, breathing rate, blood flow velocity estimation as well as variations of flow distributions over time during bleeding and resuscitation stages. Our work can enable new research in critical care, helping correlate heart rate and breathing cycle with flow distributions and studying effects of interventions and protocols in real-time for bed-side patient care. In comparison, most previous works either included significant manual interactions and were not real-time, or are tailored to high quality 2D images or 3D volumes that do not work for SDF videos.

The underlying principle of our approach is that diagnostically useful information must be extracted quickly, enabling the user to make determinations about microcirculatory flow in real time, rather than off line as is done currently, and ultimately enable making clinical decisions instantly at the bedside. To this end, we present a framework consisting of multiple stages including video stabilization, enhancement, micro-vessel extraction and automatic estimation of the micro blood flow statistics from SDF videos.

Our method has been used in a critical care experiment conducted carefully to analyze the microcirculatory blood flow of subjects in different health conditions. In the experiment, healthy pigs have been anesthetized and subjected to induced slow bleeding (20 ml/min) for about 2 hours. Then the subjects were fluid resuscitated to expand the plasma volume. Microcirculatory videos were captured at different stages of the experiment to monitor changes in the micro blood flow. 96 videos of 18 pigs were collected using a SDF imaging device for each bleeding/resuscitation stage. Our method was then applied to extract physiological information from the videos. As a result, the extracted informative microcirculatory features form distributions that are consistent with the intuition of expert clinicians.

II. RELATED WORK

Image based microcirculatory blood flow assessment have been studied using Laser speckles [2], [3]. More recently, skin perfusion measurement based on laser speckle was proposed in [13]. Instead of images or videos of the microcirculatory blood flow, these methods leverage complex speckle patterns. In Sidestream Dark Field imaging system [7], microcirculatory blood flow is analyzed based on the vessel detection from video while the detections of vessels is refined with expert interface [6]. In [5], the vessel segmentation using the microcirculation is present. Then the blood flow characteristics are extracted by using the intensity changes of individual pixels on the vessels. To get the blood flow status from micro-circulation video, template-matching method [?] and mode tracking in the spatial temporal space [17] have been used to deal with the highly variant changes of the shape and brightness of RBCs.

A complete review of different techniques for bedside micro-circulation analysis can be found in [1].

The vessels in the image are often detected as centreline structures [15], [19], [14], [10], [12] either by using filters [19], [10], intensity profiles [15], [12], or trained regressors [14]. Then, level-set methods are used to locate the centreline more precisely [9], [20].

In [16], various optical flow approaches are studied. It was shown that by using an objective with a non-local term, the classical optical flow formulations can achieve competitive results. For motions of deformable objects, the motion estimation problem is often formulated as optimization solved by inverse compositional image alignment [11], supervised-learning of descent direction [18], and data-driven descent [18]. In our case, with high level of noise, highly deformable blood flow patterns, and small dimensions of capillaries, it is very difficult to track the flow on a frame-by-frame basis.

To get motions that are more obvious and easier to detect, video motion magnification method has been proposed in [22]. Extensions have been put forward to either reduce the noise in the motion magnified video [22] or achieve real-time running speed [21]. Because of the high level noise in the SDF videos, applying any of those methods directly would likely amplify the noise as well.

III. CRITICAL CARE CASE STUDIES

To study the effect of the fluid resuscitation process on the living subjects with hemorrhage, critical care experiment on living pigs is conducted carefully. The critical care experiment procedure is shown in Fig. 2. All experiments were performed in accordance with NIH guidelines under protocol approved by the Institutional Animal Care and Use Committee of the University of Pittsburgh. Three Yorkshire Durock pigs (average weight of 30.6 kg) were fasted overnight prior to the study. Anesthesia and the surgical preparation have been performed following procedures described in [8]. Briefly, following induction of general anesthesia and endotracheal intubation, arterial and central venous catheters were inserted and the animals allowed to stabilize for 30 minutes. During this time the SDF probe attached to a vise clamp was positioned in the pigs mouth under the lounge to visualize the sublingual microcirculation. Care was taken to obtain a long-term stable image with minimal pressure artifact and good visualization of the microcirculation as defined by the optimal focal length and illumination to visualize the largest number of capillaries within the viewing frame as previously recommended in [4]. At the end of the baseline period the initial video was collected (Baseline). All videos were 20 seconds in length at 10 frames per second. Then the pigs were bled from the arterial catheter at a fixed rate of 20 ml/min until the mean arterial pressure decreased to 30 mmHg. Once at this pressure, bleeding was stopped and a second video was captured (EndBleed). The subject was kept in this hypotensive state for 90 minutes with video images captured at 60 minutes into the hypotensive state (AfterBleed) and again at 90 minutes (BeforeResusc). Then the pigs were fluid resuscitated with Hextend (equal volume to shed blood) at 60 ml/min. At the end of this fluid resuscitation

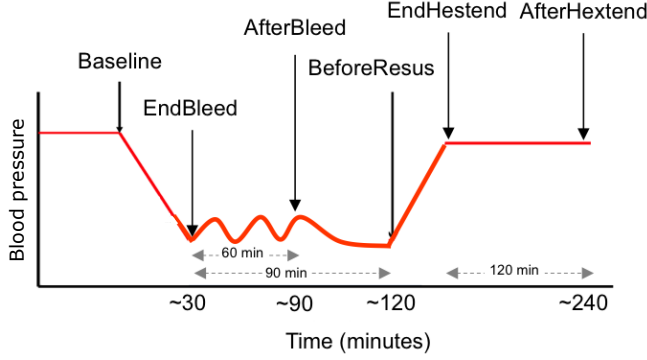


Fig. 2: Setup of the experimental procedure. 18 pigs are observed carefully at various stages of bleeding and resuscitation.

period another video was captured (EndHextend). Then the animal was further resuscitated in a protocolized fashion as previously described with more fluid if the cardiac output was less than baseline and norepinephrine if mean arterial pressure was less than baseline for an additional 120 minutes and a final video image was taken (AfterHextend). Since many animals became unstable before 90 minutes of hypotension or did not survive 120 minutes after the start of resuscitation, some animals did not have BeforeResusc and AfterHextend time point videos collected. So, a 20-second microcirculation video clip was captured at each of the six stages described above: (1) Baseline: right before the bleeding; (2) EndBleed: at the end of bleeding; (3) AfterBleed: 60 minutes after the end of bleeding; (4) Before resuscitation: 90 minutes after the end of bleeding; (5) End of resuscitation: the end of the resuscitation process, in which the Henxtend fluid is infused intravascularly; (6) After resuscitation: end of observation period.

IV. MICRO-VESSEL EXTRACTION FROM VIDEO

The contrast of the SDF images is greatly reduced by the presence of the subsurface scattering and sensor noise. This makes it difficult to detect the capillaries from any single frame in the video. One option is to detect the capillaries from the minimal image, where the values of the pixels are set to the minimal intensity across frames at that pixel location. However, the input videos are not stable because of motions introduced by heart beat, respiration, and sensor position drift. So we need to stabilize the video before extracting vessel skeletons.

A. Video Stabilization

After motion due to heartbeat, breathing and sensor position drift is eliminated, the stabilized video will mainly consist of the blood flow in the capillaries. For efficiency considerations, we base video stabilization on motions of the patches that are corresponded between frames using template matching. Since the microcirculatory videos are captured carefully to avoid unnecessary motion of sensor relative to subject, frame-to-frame changes are limited and smooth. Thus the correspondence between patches in different frames can be estimated. In addition, patch-based stabilization method enables including

variations of the patch motions in a frame introduced by deformable properties of the tissue.

Because the videos are effectively textureless in most parts of the frames, we need to select the optimal patches for finding correspondence in the stabilization process. In our method, we select the patches in which the variance of intensities is above a pre-set threshold such that the selected patches include enough texture for matching.

Heartbeat and respiration rates can be obtained as side products of the video stabilization process. Those physiological measurements can be used along with the microcirculatory blood flow parameters, to further aid diagnosis and monitoring processes. As the observed motion introduced by the heart beat and breathing also depends on the location where the microcirculatory videos are taken, the measured motion can be used as a guidance for the clinician to determine the location of target tissue considered for diagnosis. In addition, although in clinical practice the assessment of the heart rate and the respiratory rate already exist via dedicated, specialized monitors, it is not known whether and how their variations impact physiology of tissue blood flow. The measurements of these signals thus provides an opportunity to study these interactions in a live subject concurrently with flow information, and generate further knowledge in the field.

We decompose the observed cross-frame motion into heartbeat and respiration motions based on their frequencies. More specifically, the respiratory is the motion component in the [.1 , .5] Hz frequency range in the Fourier transform of the averaged observed motions of patches in the un-stabilized video; and the heartbeat is the motion component in the [.5 , 5] Hz frequency range. In the corresponding frequency ranges, the frequencies of the heartbeat and respiration motions are determined as the frequencies where the local maxima of magnitude in the Fourier domain occur. The magnitudes depend on the status of the subject and the location where the video is taken. For Pig 42, as shown in Fig. 3(a), most of the observed motion is due to the heartbeats. For Pig 44 at the end of bleeding, both the respiration and heartbeat motions are more significant. For Pig 44 before bleeding, the sensor drifting dominates the observed motion, while the other two components can still be reliably identified. This last observation has important practical implication, since apparently the perfect stabilization of the sensor probe against the subject tissue is not necessary for extracting reliable physiological information from SDF imaging videos.

B. Vessel skeleton extraction

After stabilization, we have registered frames from which the skeletons of vessels can be extracted. However, as shown in the first column of Fig. 4, due to subsurface scattering and imaging noise, the contrast in individual frames is too low for extracting vessel segments. Even worse, the transparent plasma travelling through the capillaries may make vessels invisible in some segments of a frame. So we first need to produce a vessel-enhanced image. Based on the fact that the capillaries with red blood cells are usually darker in the frames, we can take the minimal value of each pixel across all the frames to

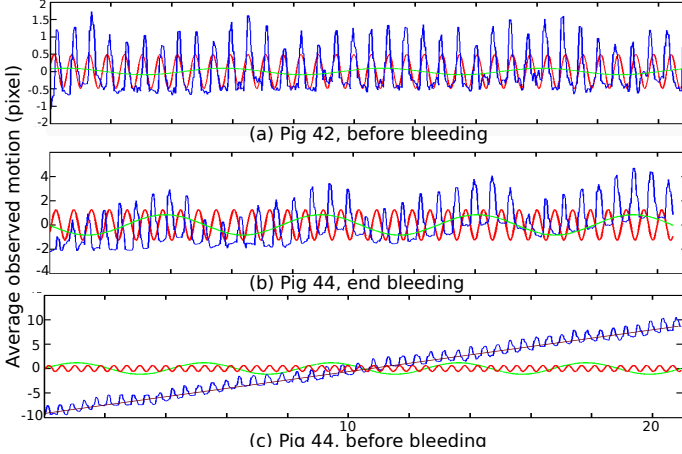


Fig. 3: The heartbeat and breathing rates are evaluated by decomposing the averaged observed motion (blue) across frames into heartbeat and breathing motions, shown in red and green respectively. For measurements with sensor drifting, we also get the motion component due to sensor drifting (shown in brown). (a) Pig 42 at the end of baseline (before bleeding). Most of the observed motion is due to the heart beat. (b) Pig 44, end of bleeding. Both heartbeat induced motion and breathing motion are obvious. (c) Pig 44, baseline. The sensor position drift (shown in brown) dominates the averaged observed motion, but the physiologic components can still be clearly identified.

achieve that goal. This method works under assumption that for every pixel of the vessel there is at least one frame in which a red blood cell passes through it. This assumption is true for most cases since the duration of the microcirculatory videos (20 seconds) is long enough for the red blood cells to pass through all the active vessels in the frame.

Then the vessel enhanced image is denoised by applying anisotropic diffusion filtering. It not only reduces the imaging noise while leaving the edges in the vessel enhanced image unharmed, but it also smoothes the parts of the image along the structures between the edges. This results in vessel segments with a smooth appearance so they can be detected more easily. The filtered vessel enhanced images are shown in the second column of Fig. 4.

To detect the vessel skeletons, we first estimate the Hessian matrix for each pixel in the vessel enhanced image. Then the profile for each pixel is extracted along the direction of the eigenvector of Hessian corresponding to the largest absolute eigenvalue. The pixel will be selected as a vessel skeleton pixel if the profile has a groove in the middle and increases towards both sides of the groove. To find the vessel skeletons with such profile, we use the method proposed in [15] that was designed to find the centreline of curvilinear structures.

Let $\mathbf{n} = (n_x, n_y)$ with unit length be the direction in the eigenvector of the Hessian Matrix H corresponding to the largest eigenvalue. The second-order Taylor expansion of pixel at \mathbf{x} along \mathbf{n} is given by:

$$p(t) = r + r_n t + \frac{1}{2} r_{nn} t^2 \quad (1)$$

where $p(t)$ is the pixel intensity at the position $\mathbf{x} + t\mathbf{n}$; r , r_n and r_{nn} are the pixel intensity at \mathbf{x} , the first-order derivative of the intensity in the direction \mathbf{n} and the second-order derivative of the intensity in the direction \mathbf{n} respectively. For a profile across the vessel, The center of the groove is located at the zero crossing of the first derivative of the profile:

$$t = -\frac{r_n}{r_{nn}} = -\frac{\nabla \mathbf{r}^T \mathbf{n}}{\mathbf{n}^T H \mathbf{n}} \quad (2)$$

where $\nabla \mathbf{r}$ is the gradient of the image at \mathbf{x} . In the image coordinate, the offset of the zero-cross from \mathbf{x} is $(p_x, p_y) = (t n_x, t n_y)$, with t estimated in Equation.2. The pixel \mathbf{x} is on the vessel skeleton if $|p_x| \leq \frac{1}{2}$ and $|p_y| \leq \frac{1}{2}$. To eliminate the falsely detected vessels introduced by imaging noise, we use the maximum eigenvalue of the Hessian matrix to select the detected vessel skeletons.

The example results of the skeleton extraction are shown in Fig. 4. By comparing with the vessels manually labeled by human experts , we find that the vessel skeleton extraction method is able to locate most of the vessels in the frame. Although there is a potential for a few missing and false detections, the main objective of our work to extract informative statistics of the physiological importance, and not the analysis of the individual vessels - should not suffer much. Hence, the obtained skeletons can be used as reliable inputs to the subsequent processing steps.

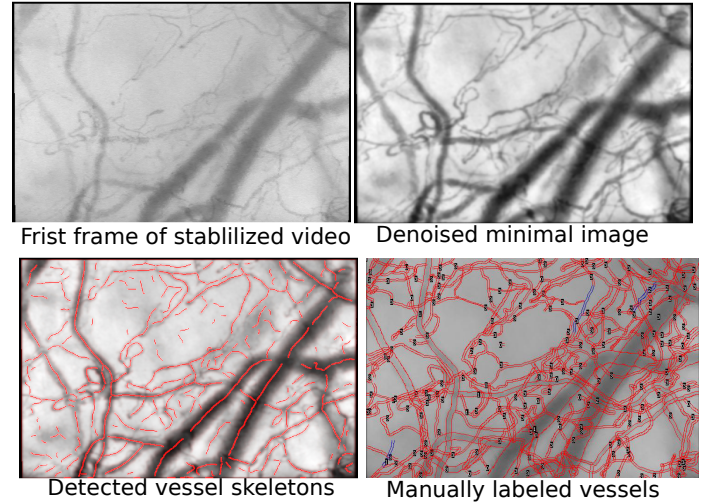


Fig. 4: The vessel skeletons are extracted from the minimal image across the frames. Upper left: the first frames of the video for Pig 53. Due to subsurface scattering and transparency of plasma, it is hard to detect capillaries from a single frame. Upper right: denoised minimal image across all the N frames. In our case $N = 200$. Lower left: extracted vessel skeletons. Lower right: manually painted vessels.

V. DETERMINE FLOW SPEED DISTRIBUTIONS AND LOCAL FLOW TYPES

The analysis of local blood flow motion pattern serves as an important aspect to assess the response of the micro-circulation system to the hemorrhage and resuscitation processes. For

example, the cardiorespiratory insufficiency caused by blood pressure loss is usually spatially variant. Such spatial variance demonstrates how the local micro-circulation system reacts to the blood pressure reduction. To visualize the spatial variance in the change of blood flow, we have designed the motion features to represent the local flows motions based on 3D convolution with pre-defined spatial-temporal filters. On top of that, a cascade of classifiers are trained to distinguish between different flow types, enabling us to localize the abnormal flows due to loss of blood pressure.

A. Motion Features

The presence of high-level noise and lack of texture inside the capillaries make the optical flow method fail in testing video for estimating the local flow motion. Two consecutive frames of a local region in one of the testing videos are shown in Fig (5) (a) (b). The optical flow estimation from those two frames is shown in Fig. (5)(c). To deal with the noise and lack of texture, we propose to use the pre-defined spatial-temporal filters to extract the local motions.

To reveal the spatial-temporal structure of the blood flow, we used the second order derivative of a Gaussian function $G_\theta(x, y, t) = \frac{\partial^2 G}{\partial \theta^2}$ where $G(x, y, t) = e^{-(x^2/\sigma_x^2 + y^2/\sigma_y^2 + t^2/\sigma_t^2)}$, θ is the direction of the gradient in the spatial-temporal domain. In addition to $G_\theta(x, y, t)$, the Hilbert Transforms of the second-order derivatives $H_\theta(x, y, t)$ are included in the filter bank. In our experiment, the filter bank spans 16 spatial orientations corresponding to vessel segments of different directions and 11 temporal orientations corresponding to different blood flow speed levels. Please refer to the supplementary material for more details about the spatial-temporal filters we used in our experiments.

The noise in the video is assumed to be *i.i.d* random and uncorrelated among different pixels, the spatial-temporal filtering will suppress the noise. On the other hand, high response will be generated if the local flow motion is close to the motion pattern of the applied filter, as shown in Fig. (5)(d). Another benefit of using the spatial-temporal filter is that by adjusting the size of the spatial-temporal filters, we are able to get localized filter responses both spatially and temporally. The prior knowledge about the vessel structures leads us to design the filters of appropriate elongated anisotropic shapes, rather than using isotropic filters.

With the location denoted as x , the speed level s and time t the filter response $m(x, s, t)$ for two points marked in Fig. (5)(d) are shown in Fig. (5)(e)(f), revealing the approximate speed of the flow as a function of the video frame and the key video frames in which there is observable blood flow passing by that point. The flow motion direction is parallel to the vessel direction estimated from the minimal image.

Given the filter response $m(x, s, t)$, the weighted kernel density of the speed across all the frames is calculated. For simplicity of denotation, the dependence on the location x is ignored in the followings. For each frame, the weighted average speed level $\bar{s}(t)$ is first estimated by:

$$\bar{s}(t) = \frac{\sum_i m(s_i, t) s_i}{\sum_i m(s_i, t)} \quad (3)$$

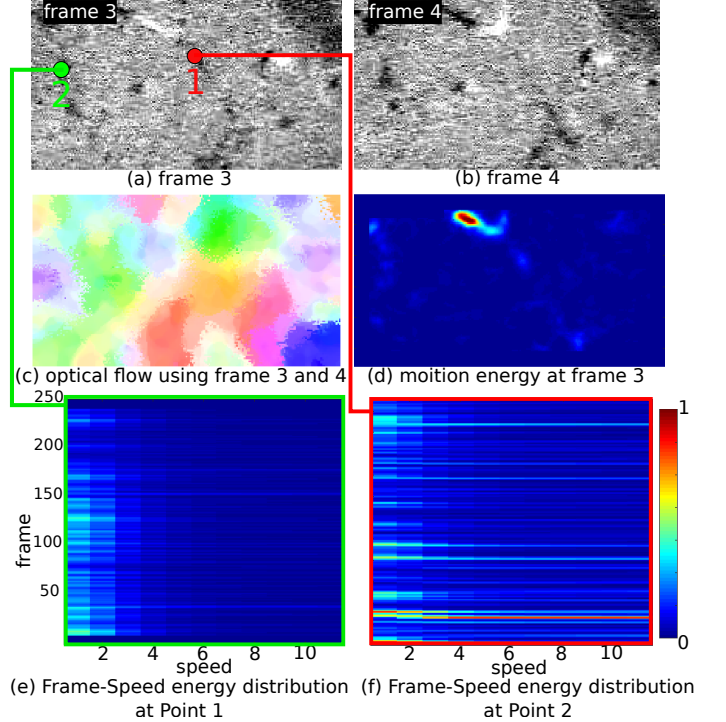


Fig. 5: Local motion estimations on a zoomed-in region of the motion magnified video showing the micro-vascular blood flow. (a) The zoomed-in region in frame 3 of the motion magnified video; (b) The same local region as in (a) in frame 4 ; (c) The estimated optical flow using the two frames in (a) and (b); (d) The overall motion energy calculated from the filter response. The flow motion induces high motion energy while the motion energy for the noise is low since the artifact motion patterns introduced by noise are not aligned with any of the applied 3D filters. (e)(f) The filter responses at the marked points in (a), revealing the approximate speed of the flow and the key frames in which there is observable blood flow passing by those locations.

with $s_i = \{0, 1, \dots, 10\}$, i.e., 11 blood flow speed levels. The weight for the average speed level is determined as the motion energy $m(\hat{s}, t)$, where \hat{s} is the closest speed level to \bar{s} . The weighted kernel density of the speed $f(s)$ is:

$$f(s) = \frac{\sum_t m(\hat{s}, t) \varphi_h(s - \bar{s}(t))}{\sum_t m(\hat{s}, t)} \quad (4)$$

where $\varphi_h(x)$ is the kernel function with bandwidth h . In our case we use the Gaussian kernel functions. The weighted kernel density of the speed $f(s)$ is used as the per-pixel motion feature. The motion feature at three locations where different flow types passing by is shown in Fig. (6). Point 3 is located on a capillary with normal flow while point 1 and point 2 are located on capillaries with abnormal intermittent flows due to loss of the blood pressure. The intermittency of the flow at point 2 is greater than that for point 1. This has been reflected in the motion feature in Fig. (6) (b): the kernel density for point 2 spans a wider support than point 1, while almost all density for point 1 is concentrated at a narrow range of speed level.

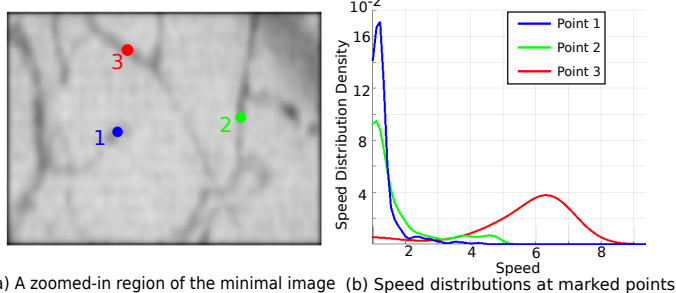


Fig. 6: The speed level distributions at three points. The corresponded points and speed level distributions are plotted in the same color. Point 3 is located on a capillary with normal flow. Point 1 and Point 2 are located on capillaries with stopped and intermittent flows respectively.

B. Blood Flow Types

We have presented the method to measure the overall flow speed distribution in the video. In addition that, in the next sections, we present the method of estimating the *local* flow speed for *every single position* in the video. This has enables us to determine the spatially variant flow type across the field of view, as shown in Fig. 10.

The flow inside the capillaries will decrease in dynamics due to the blood pressure reduction in the hemorrhage process. As a result, the health status of the subjects can be inferred from the changes in the motion pattern of the blood flow. To better quantify and visualize the flow motion pattern changes, based on the clinical experience we define three types of flows: stopped flow, intermittent flow and normal flow. For the stopped flow, the blood within the capillaries has little or no motion either because the blood pressure is insufficient or due to the external pressure introduced by the contact with the measurement device. The intermittent flow includes the flows with unstable flow speed. Usually the flow speed varies within the low speed range. The normal flow are the flows with fast and consistent motion patterns. Therefore, the speed level distribution of stopped and normal flows are uni-modal while the intermittent flow is bi-modal or multi-modal and spans a wider speed range than the stopped flow, as shown in Fig. 6(b).

To visualize the spatial distribution of flow types, we have defined the score functions for the stopped and intermittent flows. The normal flow is complementary to the stopped and intermittent flows. In other words, we will consider the flow with low stopped flow and intermittent flow scores as normal.

The score function for the stopped flow is defined as:

$$v_{\text{stop}} = -(I_{\min}^2 + \lambda_1 \sigma_t^2 + \lambda_2 \bar{s}^2), \quad (5)$$

where I_{\min} is the minimal frame value, σ_t is the intensity variance across all frames; \bar{s} is the mean speed level defined in Eq. 3. The first two terms simply reflect the fact that the flow is static. In the third term, we take into consideration of the tiny motions in the static flow.

The score function of the intermittent flow is defined as:

$$v_{\text{int}} = \frac{\sum_{i=1}^2 f(s_i)}{\sum_{i=1}^{11} f(s_i)} \quad (6)$$

, where $f(s_i)$ is defined in Eq. 4. Although the definition simply consider the ratio of low speed level in the overall motion pattern, the intermittency of the blood flow can be fairly measured indirectly, as can be seen by comparing the intermittent flow score map for Pig. 55 in Fig. 7 and the flow type classification results shown in Fig. 10 using the learning-based method introduced in the next section. More comparisons between the intermittent flow map score and the classification results can be found in the supplementary material. The reason why this simple definition for the intermittent flow performs well is that the flow speed variations usually happen within the low speed range. In other words, the blood flows in high speed levels are stable at the same time.

C. Supervised Method

Although we are able to quantify the degree to which type the flow belongs based on the scoring functions defined above, it is not guaranteed that the three types flows are mutually exclusive since the scoring functions are defined separately and in a heuristic manner. So in addition to using the manually defined scoring functions for different types of flow, we also propose a learning-based method with cascade classifiers. To this end, we have labeled all the 97 micro-circulatory videos of the 18 pigs in the experiment. For each video, a subset of vessels/background area are labeled as one of *stopped*, *intermittent*, *normal* flows and *background* classes. Examples of the labeled video are included in the supplementary material.

In the first stage, vessels are separated from the background based on the local structure information encoded in the spatial structural feature:

$$\mathbf{l}_1 = [I_{\min}, \sigma_t, \text{foof}(k_i; I_{\min}), \dots, \text{foof}(k_i; \sigma_t) \dots] \quad (7)$$

, where I_{\min} is the minimal image, σ_t is the intensity variance map across all frames $\text{foof}(k_i; I_{\min})$ is the Optimal Oriented Flux filter [10] response at scale k_i operated on I_{\min} .

In the optional second stage, wide vessels are removed and the flow patterns in those wide vessels are not considered as capillaries in the following stage. During the measurement process, the wide vessels are used to locate the region where the video is being captured by clinicians. Also, since the wider vessels are located deeper below the surface than the capillaries, they are usually out-of-focus given the small depth of focus of a micro-scale lens. Thus the evaluated motion patterns in the wide vessels are not reliable due to the blurring effect. In the second stage, we use the same feature as in the first stage to represent local structure information.

In the third stage, the blood flow within the detected vessels are categorized into stopped, intermittent and normal flows. The features of flow type determination is the concatenation of speed level distribution evaluated using Eq. 4 along with the local structural features:

$$\mathbf{l}_3 = [\mathbf{f}(s), \text{foof}(k_i; I_{\min}), \dots, \text{foof}(k_i; \sigma_t) \dots] \quad (8)$$

, where \mathbf{f} is the speed distribution defined in Eq. 4. We use the Random Forest Classifiers in all three stages.

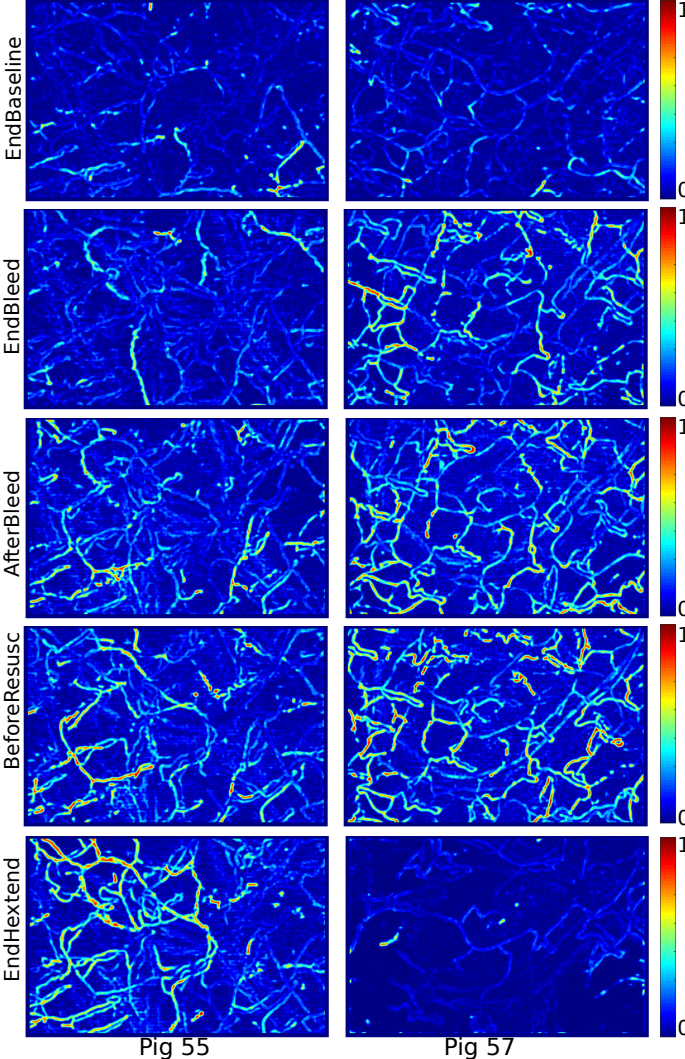


Fig. 7: The score function map for intermittent flows for Pig 55 and Pig 57 in different stages. For both pigs, the vitality and blood pressure loss during bleeding is reflected by the increasing in the intermittent flow from EndBaseline to BeforeResusc. The difference in the response to the resuscitation process for two pigs is reflected in the score function map at the EndHextend stage: For Pig 57 the intermittent flows reduces dramatically while for Pig 55 the resuscitation did not help to recover the capillary blood pressure hence the intermittent flow becomes even more prevalent.

Compared with a one-stage classifier which directly categorize the pixels into background and three types of flows, the cascade classifier emphasizes different types of features in stages. For the task of separating the vessels from the background, the statistics of the video such as the minimal image provides more structural information than the raw frames from the video, given the poor imaging quality and lack of texture to detect the curvilinear structures in the raw video. Therefore, the structural features extracted from the minimal image is more appropriate than the motion features extracted from the video for the task of extracting the vessel-like structures. On the other hand, the motion features are

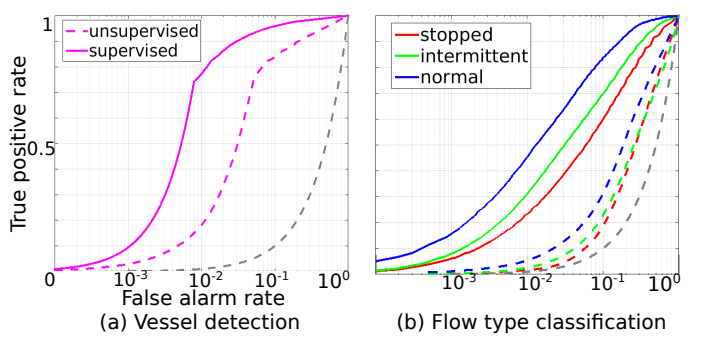


Fig. 8: The performance comparison between the supervised method (Section. V) and unsupervised method (Section. IV) on the task of extracting the vessels and classifying the flow into stopped, intermittent and normal flow. The performances are evaluated by training the cascade classifier on labeled samples from one set of pigs and test on the samples from another set of pigs. (a) The performances on the first stage of the cascade classifier where the vessels are detected. (b) The performances on the second stage of the cascade classifier where the blood flow within the detected vessels are categorized into three types of flows (stopped, intermittent and normal).

necessary for the task of categorizing the motions of blood flow into different types.

The performance of the cascade classifier is tested on the labeled data. For the first stage where the vessels are segmented from the background, we compare the performance of the supervised method introduced in this section with the vessel skeleton extraction method described in Section. IV. For the third stage, we compare the performance of the method based on the score functions for different types and the supervised method. The performances are evaluated by training the cascade classifier on labeled samples from one set of pigs and test on the samples from another set of pigs. The comparison in terms of the ROCs are shown in Figure. 8. For both detecting the vessel and categorization of the flow type, the learning-based method performs better than the method based on manually defined score functions.

To evaluate the robustness of the features and the learned classifiers, we train and test the cascade classifiers in three cases with different rules of selecting the training and testing set: (1) The training and testing samples are selected randomly from the labeled data without any constraints; (2) The samples are selected such that the training and testing samples are on different vessels; (3) Training and testing samples are selected from videos of different pigs. In the second and third cases, we consider the influence of the variance in locations and subjects. The performance is evaluated in terms of the third stage in the cascade classifier and shown in Figure. 9.

VI. PHYSIOLOGICAL ANALYSIS FROM VIDEO

In this section we will relate the estimated blood flow velocity distribution and flow types of all vessel segments detected in the field of view, to the status of the test subjects in the bleed and resuscitation phases of the experiments in

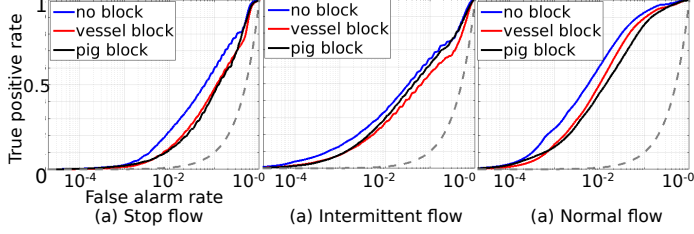


Fig. 9: The ROCs evaluating the flow type classification on the testing sets for three cases of train/test sample selection: No block - The training and testing samples are selected randomly from the labeled data without any constraints; Vessel block - the samples are selected such that the training and testing samples are from different vessels; Pig block - the samples are selected such that the training and testing samples are from videos of different pigs. (a) The performance on the stop flow; (b) The performance on the intermittent flow; (c) The performance on the normal flow.

order to evaluate consistency of our method with knowledge and intuition of expert clinicians.

From the point of view of current knowledge of physiology of the observed processes, as the blood pressure decreases due to bleeding, a general reduction in blood flow velocity is expected. It should be manifest in the flow velocity distributions by a shift of the distribution of velocities across vessels towards lower values of velocity, as well as the reduction in the population of the normal flow type and increase in the abnormal flow types (intermittent and stopped flows).

Although resuscitation should intuitively lead to an increase of microcirculatory flow, the temporal relation between restoration of arterial pressure and cardiac output to microcirculatory flow is complex and not yet fully understood. Still, one would expect that if resuscitation efforts were successful, that microcirculatory blood flow would return to baseline values. Other sources of variations in the blood flow velocity and types come from the artifacts introduced during capturing such as the contact pressure of the device and the change of locations being measured. The distributions of the blood flow velocity and the ratios of different flow types estimated from the corresponding videos are consistent with the above intuition. The analysis visualization for five pigs are shown in Fig. 11.

Pig 54, Pig 44 Pig 60: The blood flow in the capillaries diminishes after bleeding as the blood pressure and the vitality of the pig deteriorate. This change has been reflected in the figure as the flow velocity distribution, shown in the green curve, squeezes towards a lower values. In addition, the number of capillaries with slow flow velocity decreased after resuscitation as compared to the after bleed phase. In terms of the flow types evaluated using the cascade classifier, it can be observed that the ratio of the normal flow decreases while the ratios of the intermittent and stopped flow grow during the bleed phase. On the other hand, during the resuscitation phase, the normal flow ratio comes back and recovers to the level close to the baseline stage. This is consistent with physiologic expectations, and represents the opening of capillary beds

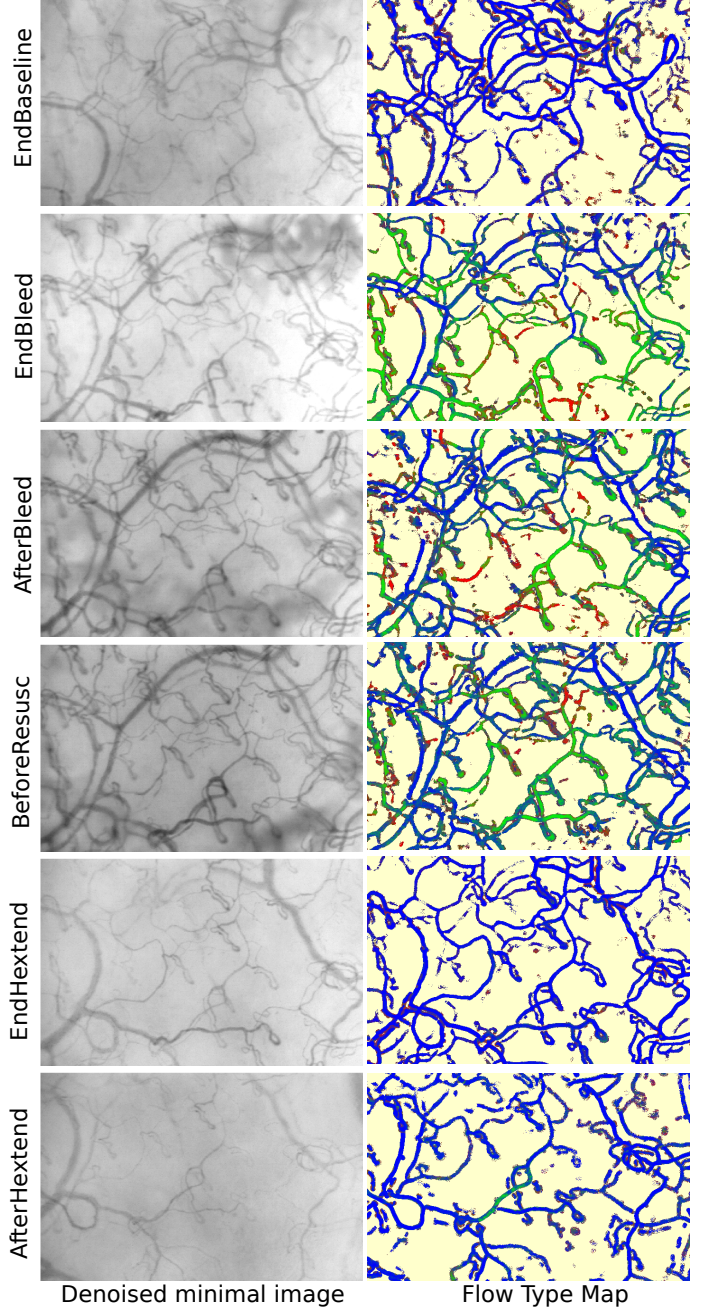


Fig. 10: The blood flow type map estimated by the cascade classifier for Pig 54 at different different stages. The color encoding for flow types: red - stopped flow; green - intermittent flow; blue - normal flow; light yellow - background. The dynamics of the blood flow in the capillaries decreases, manifested as the increasing population of stopped and intermittent flows, during the hemorrhage process. Then it recovers to normal after the resuscitation process. Those changes for the same subject are also observed from the estimations of the blood flow velocity distributions and flow type ratios, shown in the fourth row of Fig. 11.

that were previously closed probably due to insufficient input pressure during shock. Given that this protocol was intended to study the individual responses of each animal to hemorrhage,

blood volume shed was different between animals. Pig 44 and 60 had 534 ml and 760 ml blood hemorrhaged, respectively, which represented 23% and 36.7% of their calculated total blood volume. This analysis also demonstrated how for example pig 44 had a lower relative increase in capillaries with slow flow, than pig 60, which is consistent with having had a less intense response, to a less intense injury.(less volume bled).

Pig 47: it is observed in both the flow velocity distributions and flow type ratios that the flow dynamics before bleeding is within a low range. This artifact is introduced by the contact pressure of the measurement device on the tissue during capturing the micro-circulatory video for Pig 47 in the baseline stage, making the blood flow suppressed at that stage. Our method has reflected such measuring artifacts during capturing.

Pig 55: the blood flow velocity remains within a low level even after the resuscitation process, showing the difference among individual subjects in response of the resuscitation process after hemorrhage. There are only 5 stages in total for Pig 55 since that subject died before the last stage. Please refer to the supplementary material for the estimations of flow velocity distributions and flow type ratios of other subjects in the experiment.

VII. CONCLUSION

We presented a multi-stage framework for processing microcirculatory videos automatically and in real time. The processing stages include video stabilization, image enhancement, and micro-vessel extraction, in order to automatically estimate statistics of the micro blood flow captured in SDF videos. We applied our method to analyze changes in microcirculation in test animals at different stages of induced bleeding experiment, including before, during and after bleeding as well as after resuscitation. The results include both the blood flow speed and flow type distributions over the field of view and local per-pixel flow type classification based on motion features. The results show that by using image augmentation and continuous video sampling techniques, reliable microcirculatory imaging processing can be automated and accomplished in real time despite the inherent challenges to microcirculatory flow quantization. The parameters described in this analysis represent novel metrics of SDF imaging that should substantially improve the utility of SDF imaging to assess microcirculatory changes with disease and its treatment. In the future, we are going to improve the SDF imaging device such that more reliable and noisy-free data can be obtained. In addition, physiological correlations such as the flow velocity variations during different phases of heartbeat and respiration will be studied to further enhance the clinical relevance of the framework.

REFERENCES

- [1] D. D. Backer and A. Durand. Best Practice & Research Clinical Anaesthesiology Monitoring the microcirculation in critically ill patients. *Best Practice & Research Clinical Anaesthesiology*, 28(4):441–451, 2014. [2](#)

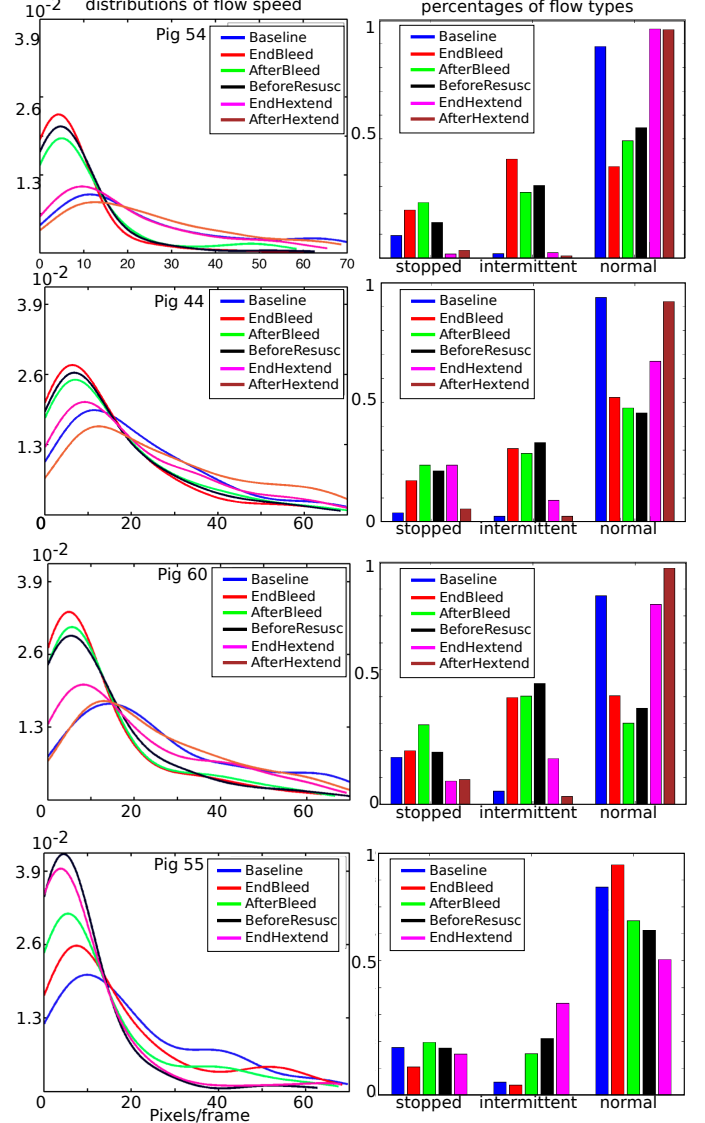


Fig. 11: The estimated blood flow velocity distributions and flow type ratios for pigs at different stages. The abbreviations for stages are described in Section. III. For Pig 54, 44 and 60, the blood flow velocity decreases and the abnormal flow type percentages increase during the hemorrhage session and recover to normal after the resuscitation process, as shown in the first three rows. For the case of Pig 47 shown in the third row, the flow velocity is low in the EndBaseline stage because of the contact pressure from the device. For Pig 55, the resuscitation failed and the pig died before reaching the last stage, as shown flow dynamics.

- [2] J. D. Briers and S. Webster. Laser speckle contrast analysis (LASCA): a nonscanning, full-field technique for monitoring capillary blood flow. *J. Biomed. Opt.*, Apr. 1996. [2](#)
- [3] H. Cheng, Q. Luo, Q. Liu, Q. Lu, H. Gong, and S. Zeng. Laser speckle imaging of blood flow in microcirculation. *Phys. Med. Bio.*, 2004. [2](#)
- [4] D. De Backer, S. Hollenberg, C. Boerma, P. Goedhart, G. Büchele, G. Ospina-Tascon, I. Dobbe, and C. Ince. How to evaluate the microcirculation: report of a round table conference. *Critical Care*, 11(5):R101, 2007. [2](#)
- [5] S. U. Demir, R. Hakimzadeh, R. H. Hargraves, K. R. Ward, E. V. Myer, and K. Najarian. An automated method for analysis of microcirculation videos for accurate assessment of tissue perfusion. *BMC medical*

- imaging*, 12(1):37, 2012. 2
- [6] J. G. Dobbe, G. J. Streekstra, B. Atasever, R. van Zijderveld, and C. Ince. Measurement of functional microcirculatory geometry and velocity distributions using automated image analysis. *Medical & biological engineering & computing*, 46(7):659–670, Apr. 2008. 2
 - [7] P. T. Goedhart, K. M. R. Bezemer, J. Merza, and C. Ince. Sidestream Dark Field (SDF) imaging:a novel stroboscopic LED ring-based imaging modality for clinical assessment of the microcirculation. In *Optics Express*, pages 1–14, Dec. 2007. 1, 2
 - [8] H. Gómez, J. Mesquida, L. Hermus, P. Polanco, H. Kim, S. Zenker, A. Torres, R. Namas, Y. Vodovotz, G. Clermont, J. Puyana, and M. Pinsky. Physiologic responses to severe hemorrhagic shock and the genesis of cardiovascular collapse: can irreversibility be anticipated?. *Journal of Surgical Research*, Nov. 2012. 1, 2
 - [9] M. S. Hassouna and A. A. Farag. MultiStencils Fast Marching Methods: A Highly Accurate Solution to the Eikonal Equation on Cartesian Domains. *IEEE Transactions on Pattern Analysis and Machine Intelligence*, 29(9):1563–1574, 2007. 2
 - [10] M. W. Law and A. C. Chung. Three dimensional curvilinear structure detection using optimally oriented flux. *Proceedings of European Conference on Computer Vision (ECCV)*, pages 368–382, 2008. 2, 6
 - [11] I. Matthews and S. Baker. Active appearance models revisited. *International Journal of Computer Vision*, 60(2):135–164, Nov. 2004. 2
 - [12] A. M. Mendonça and A. Campilho. Segmentation of retinal blood vessels by combining the detection of centerlines and morphological reconstruction. *Medical Imaging, IEEE Transactions on*, 25(9):1200–1213, 2006. 2
 - [13] G. Satat, C. Barsi, and R. Raskar. Skin perfusion photography. In *Proceedings of IEEE International Conference on Computational Photography (ICCP)*, pages 1–8, 2014. 2
 - [14] A. Sironi, V. Lepetit, and P. Fua. Multiscale Centerline Detection by Learning a Scale-Space Distance Transform. In *Proceedings of IEEE Conference on Computer Vision and Pattern Recognition (CVPR)*, pages 2697–2704, 2014. 2
 - [15] C. Steger. An Unbiased Detector of Curvilinear Structures. *IEEE Transactions on Pattern Analysis and Machine Intelligence*, pages 1–13, Feb. 1998. 2, 4
 - [16] D. Sun, S. Roth, and M. J. Black. Secrets of Optical Flow Estimation and Their Principles. *Proceedings of IEEE Conference on Computer Vision and Pattern Recognition (CVPR)*, pages 1–8, Mar. 2010. 2
 - [17] S.You;E.Ataer-Cansizoglu; D.Erdogmus; M.Massey; N.Shapiro. Microvascular Blod Flow Estimation in Sublingual Microcirculation Videos baed on a Principal Curve Tracing Algorithm. *IEEE International Workshop on Machine Learning for Signal Processing*, 2012. 2
 - [18] Y. Tian and S. G. Narasimhan. Globally Optimal Estimation of Nonrigid Image Distortion. *International Journal of Computer Vision*, 98(3):279–302, July 2012. 2
 - [19] E. Turetken, C. Becker, P. Glowacki, F. Benmansour, and P. Fua. Detecting Irregular Curvilinear Structures in Gray Scale and Color Imagery Using Multi-directional Oriented Flux. In *Proceedings of IEEE International Conference on Computer Vision (ICCV)*, pages 1553–1560. IEEE, Nov. 2013. 2
 - [20] R. Van Uitert and I. Bitter. Subvoxel precise skeletons of volumetric data based on fast marching methods. *Medical Physics*, 34(2):627, 2007. 2
 - [21] N. Wadhwa, M. Rubinstein, F. Durand, and W. T. Freeman. Riesz pyramids for fast phase-based video magnification. In *Proceedings of IEEE International Conference on Computational Photography (ICCP)*, pages 1–10, 2014. 2
 - [22] H.-Y. Wu, M. Rubinstein, E. Shih, J. Guttag, F. Durand, and W. Freeman. Eulerian video magnification for revealing subtle changes in the world. *ACM Transactions on Graphics (TOG)*, 31(4):1–8, July 2012. 2